UCID--19422

DE82 021120

PLASMA-PARAMETER MEASUREMENTS USING NEUTRAL-PARTICLE-BEAM ATTENUATION*

CONTENTS

*A shortened version of this report is being submitted for publication.

PLASMA-PARAMETER MEASUREMENTS USING NEUTRAL-PARTICLE-BEAM ATTENUATION

J. H. FOOTE, A. W. MOLVIK, and W. C. TURNER

Lawrence Livermore National Laboratory, University of California
Livermore, CA 94550

ABSTRACT. Intense and energetic neutral-particle-beam injection used for fueling or heating magnetically confined, controlled-fusion experimental plasmas can also provide diagnostic measurements of the plasmas. The attenuation of an atomic beam (mainly from charge-exchange and ionization interactions) when passing through a plasma gives the plasma line density. Orthogonal arrays of highly collimated detectors of the secondary-electron-emission type have been used in magnetic-mirror experiments to measure neutral-beam attenuation along chords through the plasma volume at different radial and axial positions. The radial array is used to infer the radial plasma-density profile; the axial array, to infer the axial plasma-density profile and the ion angular distribution at the plasma midplane. In addition, input power to the plasma can be estimated from these results, and macroscopic plasma motion studied. Principal advantages of these measurements include the following: (1) They are continuous functions of time, (2) all the spatial information is obtained during a single plasma shot, and (3) they do not perturb the plasma because the unused transmitted fraction of the neutral beam is the part detected. The attenuation is determined by measuring the transmitted beam intensity in the presence and absence of the plasma. Representative results obtained by applying this useful diagnostic technique to the recently completed and successful tandem-mirror experiment TMX are included here. A total of 54 detectors grouped into three arrays, with line-of-sight spacing at the plasma as close as 2.0 cm and total continuous spatial coverage at the plasma of up to 35 cm, were used on TMX. This diagnostic method was well suited to the TMX-experiment parameters, and its application to similar experiments could be beneficial.

1. INTRODUCTION

Intense and energetic neutral-particle beams that heat magnetically confined, controlled-fusion experimental plasmas provide an additional method for measuring plasma properties. The amount of beam attenuation is directly related to the integrated density (line density) along a beam chord through the plasma.

The decrease in beam current transmitted through the plasma is primarily caused by charge-exchange and ionization processes. A beam atom can charge exchange off a plasma ion, losing an electron to the ion and becoming ionized. Once ionized, it follows a curved path in the magnetic field, deviating from the beam direction of motion. A beam atom can be similarly lost by ionization as a result of impact with a plasma ion or electron. Scattering and ionizing collisions of beam atoms with neutral particles in the plasma usually cause little attenuation because, first, the cross sections are small and, second, the dense high-temperature plasmas in controlled-fusion experiments are nearly fully ionized, thus allowing only a low neutral-particle density.

The total beam attenuation arises from integrating along the beam path over all the types of interactions and over the spatial distribution of interacting particles, with their possibly varying density and energy. By combining attenuation measurements with other diagnostic data and with plasma modeling, one can calculate values of plasma line density and then density.

We report here on the use, in magnetic-mirror experiments, of orthogonal arrays of highly collimated detectors of the secondary-electron-emission type to measure neutral-beam attenuation along chords through the plasma volume at different radial and axial positions. The attenuation is determined by measuring the transmitted beam intensity in the presence and absence of the plasma. The radial array is used to infer the radial plasma-density profile. From the axial array, one can not only infer the axial plasma-density profile but also the ion angular distribution at the plasma midplane (the central plasma plane perpendicular to the magnetic axis). In addition, input power to the plasma can be estimated from these results, and macroscopic plasma motion studied.

The principal advantages of these measurements are that:

- They are continuous functions of time and thus can yield time-continuous plasma-density profiles.

- All the spatial information can be obtained during a single plasma shot in a pulsed experiment.
- They do not perturb the plasma because only the unused transmitted fraction of the neutral beam is detected.
- The detectors are simple.
- The conversion from attenuation fraction to line density is expedited because the attenuation often only weakly depends on the plasma ion and electron energies.
- The analysis can be simply and quickly executed by digital computer.
- The large area of a heating beam can provide a good match to the plasma size, thus facilitating measurements of the plasma profile.

We have applied this plasma-diagnostic method extensively to the single-mirror-cell experiment 2XIIB [1,2] and, more recently, to the tandem-mirror-confinement experiment TMX [3,4]. Particle line densities, temperatures, and other plasma parameters in these experiments lie in a range yielding attenuation values conveniently measurable by this method. Characteristic of plasmas fueled by neutral beams, the plasmas formed were neither too thin nor too opaque to the neutral beams.

The 2XIIB experiment was the first magnetically confined controlled-fusion experiment in which intense neutral-beam fueling and heating were successfully used. Initial beam-attenuation measurements on this experiment are discussed in Ref [5], while Ref. [6] includes similar data from the earlier 2XII experiment.

In TMX, the first test was made of the tandem-mirror principle in combination with neutral-beam fueling and heating. Figure 1(a) shows a schematic drawing of the TMX magnet-coil system and of other experimental components such as the plasma shape and location of the end-cell neutral-beam sources. Figure 1(b) depicts idealized profiles, along the magnetic axis, of the magnetic-field magnitude, plasma ambipolar potential, and the density. In this experiment, the electrostatic-potential barriers established at both ends by high-density, high-temperature plasmas, which were magnetic-well confined, helped contain the larger volume, lower density, cylindrical central-cell plasma. Early TMX beam-attenuation results are given in Refs. [7,8].

In discussing the neutral-beam-attenuation diagnostic method in this article, we focus on its application to TMX, where 54 detectors grouped into three arrays were used--one array on each end cell and one on the central cell. Section 2 of this article covers the experimental apparatus for the

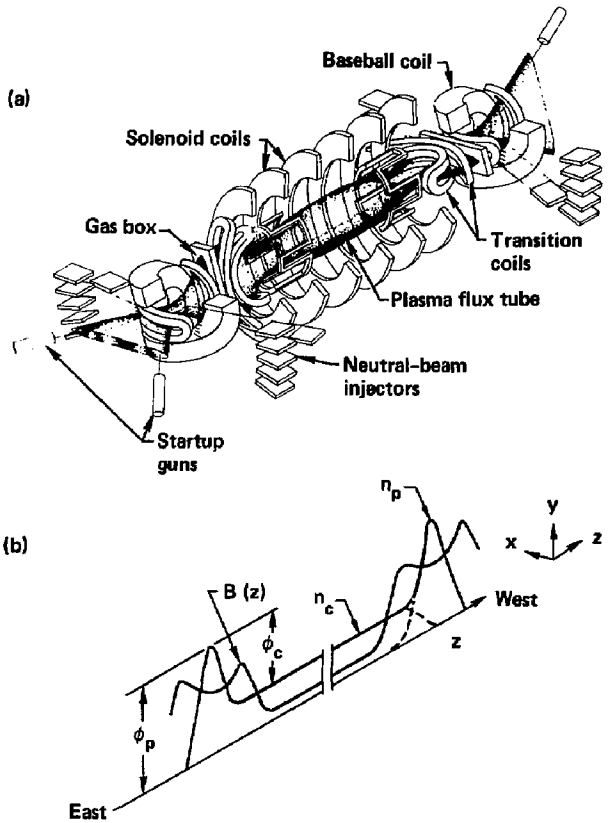

FIG. 1. Magnet configuration for TMX and profiles of axial plasma parameters. (a) Schematic drawing of magnet-coil system showing the plasma shape and location of the end-cell neutral-beam sources. (b) Idealized profiles, along the magnetic axis, of magnetic-field magnitude B, plasma ambipolar potential ϕ, and density (n_p is end-cell or "plug" density, n_c is central-cell density).

beam-attenuation diagnostic, its arrangement, and related considerations including details of the detector design and measurement accuracy. Experimental procedures for obtaining the desired data are summarized. In Sec. 3 we present representative measurement results and discuss how they can be interpreted. Some concluding and summarizing remarks are made in Sec. 4.

The neutral-beam-attenuation diagnostic has been extremely useful in the experiments mentioned above and should be helpful in related experiments. In general, the wealth of data produced by this diagnostic has been crucial in machine operation and physics understanding of 2XIIB and TMX. This method of measuring line density has tended to replace the more complex microwave-interferometry method, the two procedures usually giving consistent results.

Special beams could be installed to perform this type of measurement, but detecting the unused remnants of a fueling beam is more efficient. Early beam-attenuation plasma measurements with dedicated low-current neutral beams include those discussed in Refs. [9-14]. These measurements required momentum separation or energy analysis because of the small detector-signal levels. More recent measurements include those of Ref. [15].

2. EXPERIMENTAL METHOD

2.1. Apparatus and arrangement

Figure 2 shows schematically the basic measurement concept of the neutral-beam-attenuation diagnostic. The neutral beam passes from the source extractor grid through the plasma to the detector array. Lines representing the beam at the exit side of the plasma are lighter than those at the entrance side, denoting the attenuation in the plasma. The higher the line density encountered along a chord through the plasma, the greater the attenuation. Charge-exchange and ionization beam-plasma interactions are represented by the appearance of energetic D^+ ions in the plasma. Detectors are placed far enough from the plasma so as not to perturb it.

Each neutral-beam source used for fueling and heating TMX is similar to the type developed for 2XIIB and was designed to accelerate about 65 A of ion current at 20-keV energy [16,17]. After neutralization, about 40 A (equivalent) was incident on the TMX plasma from each source. For TMX, these sources were usually operated on deuterium gas, thus producing an

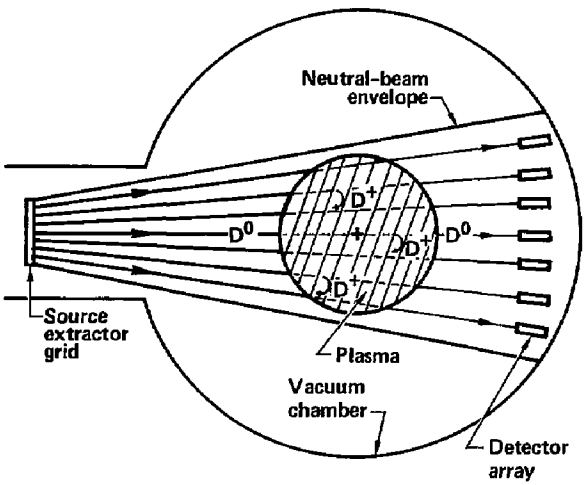

FIG. 2. Basic measurement concept and components of the diagnostic technique using neutral-beam attenuation. To depict the beam attenuation in the plasma, we have drawn thin beam lines after the plasma (to the right) and heavier lines before the plasma (to the left). The magnetic-field direction points out of the page.

atomic-deuterium beam and a deuterium-ion plasma. Their extractor-grid dimensions are 7 cm by 35 cm, and typical beam-divergence angles (at 1/e of peak power density for a bi-Gaussian beam footprint) are $\pm 0.5^{\circ}$ in the source narrow-dimension direction and $\pm 2.5^{\circ}$ in the wide. Beam composition consists of atomic components having one-third, one-half, and full beam energy produced from the breakup of triatomic, diatomic, and monatomic ions accelerated to full beam energy. Each of the three beam-attenuation-detector arrays used on TMX was focused on one of these sources.

We determined the neutral-beam attenuation by using detectors of the secondary-electron-emission type, with which we measured the flow of electrons emitted by a metal plate when it was struck by beam atoms. Alternate types of detectors might be used on other experiments, depending on parameters such as beam energy, intensity, and composition, and on the plasma environment. Secondary-electron detectors are simple in concept and use and have no moving parts. They can be small and grouped into compact arrays. No calibration is needed because the measurement is a relative one. The secondary-electron coefficient (the number of emitted electrons for each incident neutral-beam atom) must only remain constant during the time required to measure the beam intensity in the presence and absence of the plasma.

Designs of individual detectors used on 2XIIB and TMX are shown schematically in Fig. 3(a) and (b). The neutral-beam particles enter from the left in both cases, their directions being well defined by the two 0.050-cm-diam collimating holes. Baffles are located between the two limiting holes to reduce the flux of particles and photons that might scatter off the sides of the surrounding cylindrical wall and still pass through the rear collimating hole. Beam atoms striking the detector emitter surface [shown near the right side of Fig. 3(a) and (b)] knock off secondary electrons, which are then attracted to the collector element by an electrical bias that is positive with respect to the emitter. This electron-current flow, which is proportional to the incident neutral-beam-particle flux, is then measured, amplified, and recorded for analysis. An electrostatic shield surrounding the emitter-collector assembly provides protection from spurious electrical signals. The various entrance holes are open (that is, no screening material covers them).

When mounted on 2XIIB and TMX, these detectors were immersed in the experimental ambient magnetic field. Because secondary electrons spiral along

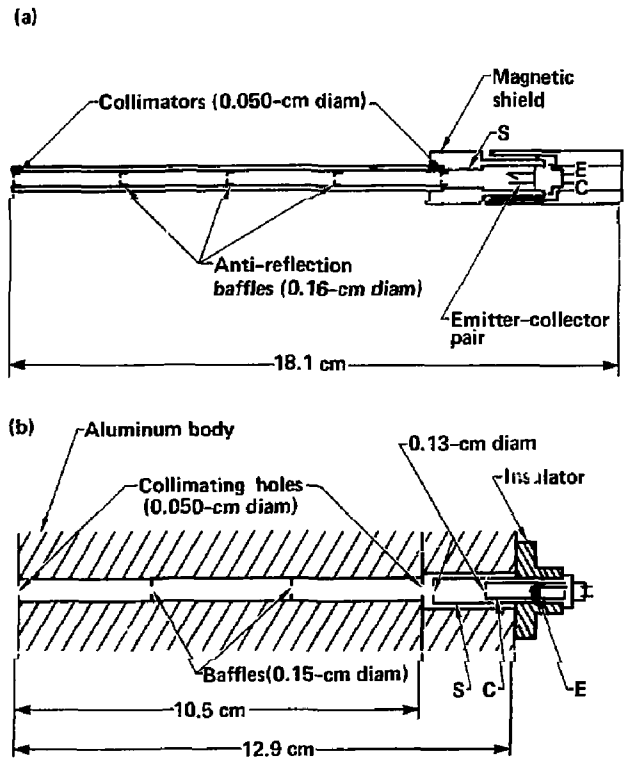

FIG. 3. Schematic drawings (approximately to scale) of individual detectors (E, emitter; C, collector; and S, electrostatic shield) used on 2XIIB (a) and on TMX (b). The neutral-beam particles enter from the left.

the magnetic-field direction, we had to either sufficiently shield a detector assembly from the magnetic field so that the electrons could freely move from the emitter to the collector or ensure that some of the magnetic-field lines always interconnected the two elements. The magnetic-field direction at the detectors on 2XIIB and TMX was somewhat uncertain because of, in particular, the influence of nearby magnetic shields around the neutral-beam sources. A small magnetic shield was used around each detector in the 2XIIB design. On TMX, we employed a cone-shaped emitter almost completely surrounded by a cylindrical collector, with no magnetic shield. The cone shape allowed at least some of the electrons to escape the emitter and reach the collector, no matter what the magnetic-field direction. Both the 2XIIB and TMX type detectors seemed to function satisfactorily.

Although details of the two detector designs differ, most features are common. For example, the detector emitter, collector, and electrical shield are made of conducting materials. Also, to minimize the perturbation of the ambient magnetic field, we used no magnetic materials in the detector construction except for the magnetic shield in the 2XIIB design. Electrically, the detector components are highly isolated to reduce leckage currents when the electrical bias is applied. Another common feature is that the emitter-collector system is constructed rigidly to maintain detector alignment and to minimize electrical noise arising from vibration-caused changes in capacity between the detector elements.

Figure 4 depicts the collimating apertures and field of view at the plasma and neutral-beam source of a detector used on the TMX end cell. The detector emitter plate lies to the right of the collimating holes and is large enough to intercept any straight line through the holes. The field of view of any point at the rear collimating hole is approximately the volume of a right-circular cone with cross-sectional diameter of 1.0 cm at the point of closest approach to the TMX magnetic axis (the axis around which the plasma is assumed centered) and with a diameter of 2.5 cm at the source extractor grid. If we allow for the finite size of the rear collimating hole, the detector field of view at the plasma has a maximum diameter of 2.0 cm and a characteristic spatial-resolution full width at half maximum of about 1.0 cm. We selected the maximum diameter of the detector field of view to be equal to or less than the spacing of the central lines of sight of adjacent detectors

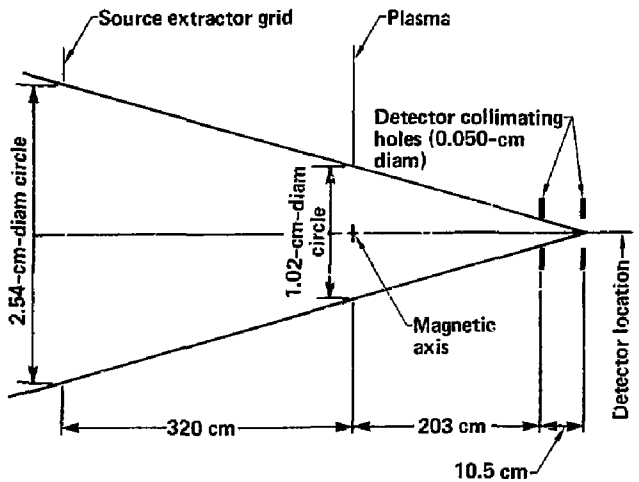

FIG. 4. Collimating holes and field of view at the plasma and neutral-beam source of a detector used on the TMX end cell (not to scale). Shown is the field of view for the center point of the rear collimating hole.

at the plasma (see below) and to be less than the smaller dimension of the extractor grid at its location.

In Fig. 5, we show central lines of sight (chords through the plasma region) for the array of 24 detectors used on each TMX end cell. Detectors were arranged in the shape of a cross with a common central detector (labeled "0" in Fig. 5) whose line of sight passed nearly horizontally through the magnetic axis at the geometric center of a TMX end cell, the approximate plasma center. The vertical and horizontal sets of detectors gave radial and axial plasma-distribution information, respectively. All detectors in the vertical set were aimed at a single spot near the center of the extractor grid (whose 7.0-cm narrow dimension was vertical) with central lines of sight spaced 2.0 cm apart at the plasma vertical plane containing the magnetic axis. The central lines of sight of the detectors forming the horizontal set were, in general, spaced at 4.0-cm intervals along the magnetic axis at the plasma and covered a total, continuous axial length of 35 cm. Most were aimed directly across the plasma at the long dimension of the grid and perpendicular to it. The perpendicular aiming maximized the signal levels. The outermost detectors were aimed inward so that their fields of view fell on the grid region.

We chose the spacings of the detector lines of sight to give adequate resolution of the plasma spatial extent anticipated in TMX and, at the same time, to require only a moderate number of detectors. This measurement technique was successful because the beam dimensions at the plasma were comparable to those of the plasma.

Figures 6 and 7 are photographs of one of the two arrays of beam-attenuation detectors used on the TMX end cells. The neutral beam approaches from the left, and the small detector units are mounted at the right extreme of the cross. The asymmetry of the cross arms was dictated by the restricted field of view through the end-cell magnet-coil system. Because the array is cantilevered, the main body is made of aluminum with holes added to further lighten it. The copper shields at the front and back help protect against electromagnetic radiation, incident-beam power, and the heat and evaporated metal from titanium gettering. In Fig. 7, two of the rear shields were removed to show the miniature two-conductor shielded cables connected to the detectors. The detector signals exit the vacuum system through individually shielded, isolated, vacuum feedthroughs (shown best in Fig. 7).

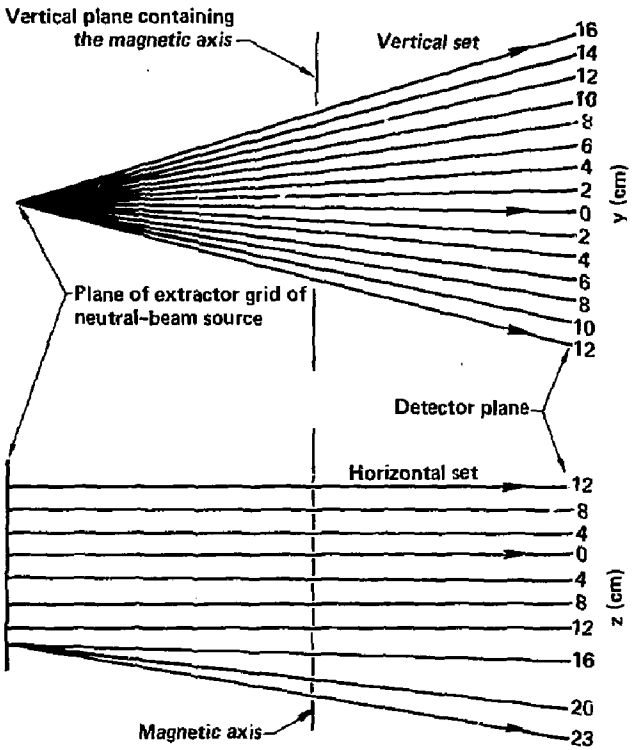

FIG. 5. Central lines of sight for the vertical and horizontal sets of detectors used on each TMX end cell. The numbers for the horizontal set (z coordinate) give the intersection positions of the central lines of sight with the magnetic axis, relative to the geometric center of the end cell. The vertical-set numbers (y coordinate) give the chord positions directly above and below the magnetic axis. The arrows show the beam-velocity direction.

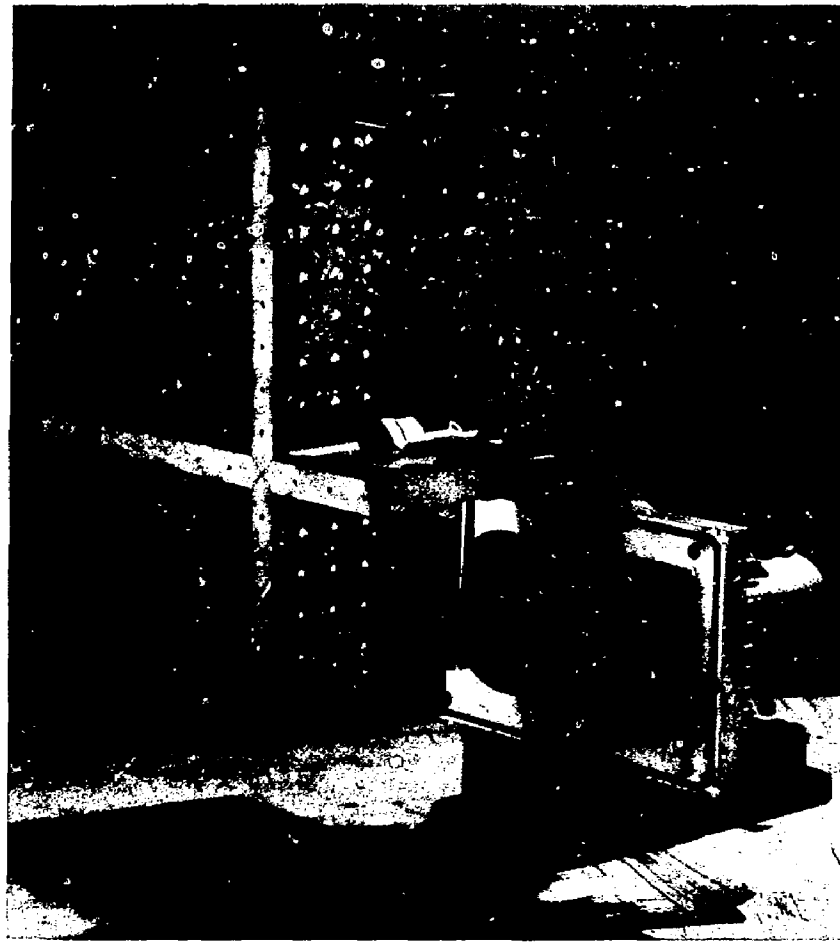

FIG. 6. Front view of a TMX end-cell beam-attenuation-detector array.

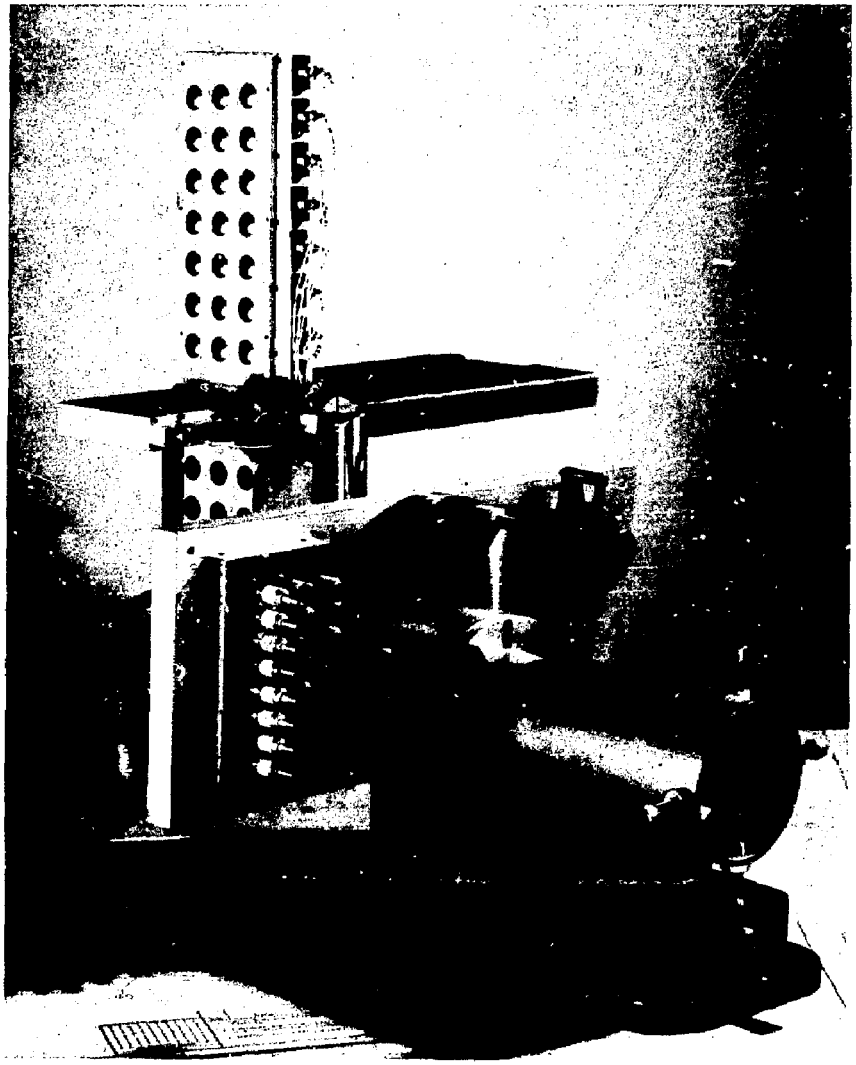

FIG. 7. Rear view of a TMX end-cell beam-attenuation-detector array.

The two sets of collimating holes for all detectors of an array were precision drilled in two thin cross-shaped pieces, which were then precisely mounted on the front and back of the aluminum body. Thus, all detector lines of sight were fixed and permanently focused on the neutral-beam extractor grid at the positions described earlier. A single alignment of an entire array sufficed to properly aim all the detectors. (Detectors were individually alignable within the array on 2XIIB.) Before mounting an array on TMX, we used a laser to check all the detector lines of sight (defined by the collimating holes) for proper aiming.

Locations on TMX of the two end-cell beam-attenuation-detector cross arrays and of the central-cell radial array are shown schematically in Fig. 8, along with other diagnostic instruments used. These many diagnostics complemented each other. For example, certain instruments provided plasma information (such as ion energy and electron temperature) needed for interpreting the beam-attenuation-detector signals. (For descriptions of the other diagnostic devices, see Ref. [4], Appendix B.) A total of 54 beam-attenuation detectors were used on TMX. The central-cell detectors were of a somewhat different design than described here, but the basic measurement technique was the same.

We now describe the manner in which an end-cell detector array was aligned on TMX and how the alignment was subsequently monitored. First, the opposite neutral-beam source was removed and a low-power laser was mounted at the location of the center of the extractor grid. With the laser aimed through the end-cell geometric center, the detector cross was positioned and aimed so that the laser beam passed through both collimating holes in front of the central detector. The array arms were then rotated to horizontal and vertical orientations. After the neutral-beam source was again mounted, the subsequent alignment monitoring was performed with another laser shining from the rear of the detector array through a set of holes in the detector cross (front hole is second from the bottom in Fig. 6) to a reference mark on the opposite side of the vacuum chamber and below the neutral-beam-source opening. The laser, which was rigidly mounted within the cylinder shown at the right in Fig. 7, moved as a unit with the detector cross. The entire apparatus could be reaimed by using three threaded adjustments, with a bellows maintaining the vacuum integrity. Pumpdown of the vacuum chamber shifted the laser-beam and detector-aiming direction by less than 0.1°, which was easily correctable.

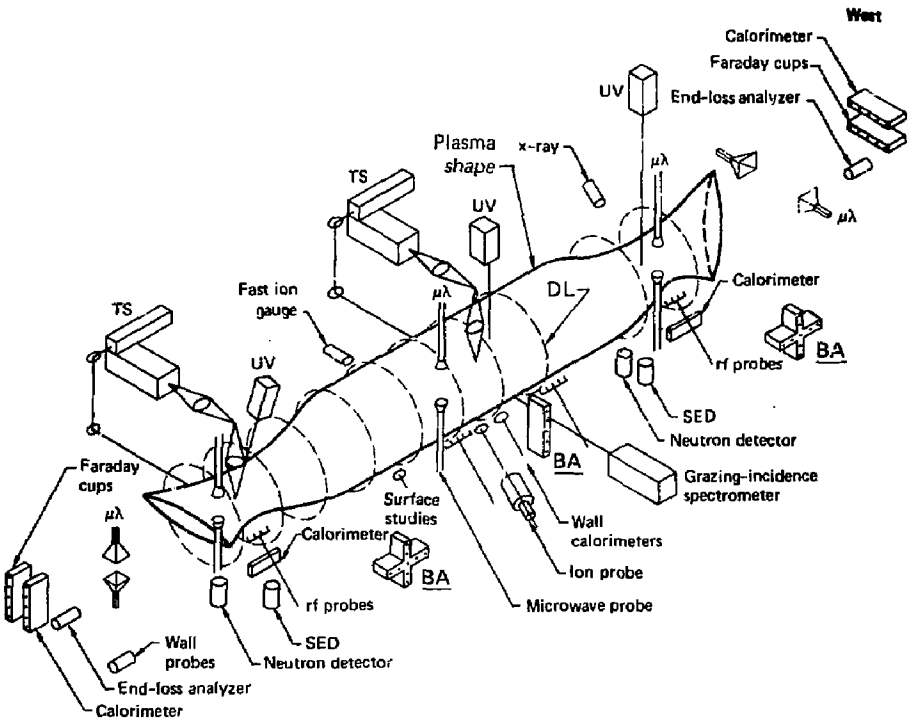

FIG. 8. Location of diagnostic instruments used on TMX, including the two end-cell and the central-cell beam-attenuation detector arrays (BA). Symbols for the other diagnostics are as follows: DL, diamagnetic loop; SED, secondary-emission detector, TS, Thomson-scattering system; UV, ultraviolet spectrometer; and μλ, microwave interferometer.

On 2XIIB, where the access was more limited, the entire detector array was aligned under vacuum by using a probe fitted with a light pipe and photomultiplier tube. The probe was aimed at a filament lamp that could be inserted in front of the neutral beam.

The electrical shielding and grounding arrangement used for the beam-attenuation detectors on TMX is shown schematically in Fig. 9. The emitter and collector leads for each detector were carried inside an electrical shield from the detector to an amplifier just outside the vacuum-chamber wall. A twisted-pair cable then conducted the amplified detector signal to the remote data-collecting area. To avoid ground-loop problems, all system grounding occurred in the remote area. The shielding and grounding arrangement was important because of the small detector signals and the noisy experimental electromagnetic environment.

Figure 10 shows schematically the principal components of the electronics system used on TMX for the beam-attenuation measurements, starting with the detector and ending with the storing of the data on magnetic tape. The amplifier had a current-to-voltage stage and a voltage-to-voltage line-driver stage. To attract the emitted secondary electrons, it also provided a +15-V bias to the detector collector element through the collector lead. The digital data recorder was triggered by a TMX-system timing pulse. It sampled the voltage signal from the amplifier unit 4096 times during or near an experimental plasma "shot" (which was about 30 ms long) and stored the values in digital form. After the shot, the computer read in the samples and stored them on magnetic tape for future analysis. Some calculation and output of line density was done between shots. The digital signals stored in the recorder were also converted back to analog form for display on a monitoring oscilloscope. A test signal could be inserted at the amplifier input to check out the electronics system.

The frequency response of this electronics system ranged from near dc (compared with the about 25-ms plasma duration) to at least the 10-kHz region. Thus, we could reliably monitor steady-state plasma behavior as well as plasma gross variations that had time behavior of up to many kilohertz. To avoid the possibility of aliasing, in which the recorded signal becomes a distorted version of the original, we limited the system frequency response and coordinated it with the digital-data-recorder sampling rate.

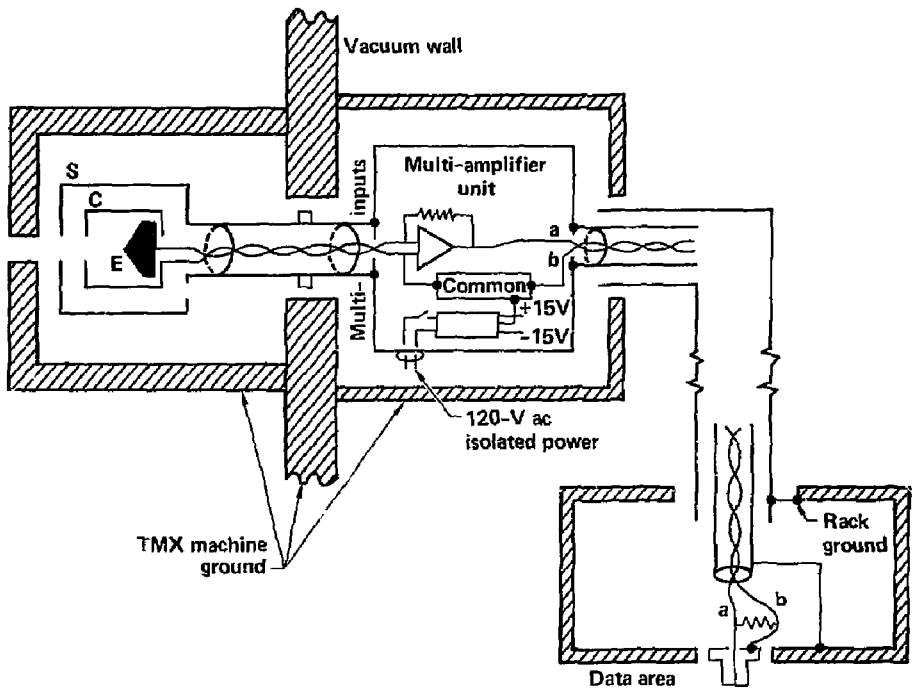

FIG. 9. Schematic drawing of the electrical shielding and grounding arrangement used for the TMX beam-attenuation detectors (E, emitter; C, collector; and S, electrostatic shield). The bundle of individually shielded twisted-pair cables that carry the detector-array signals to the remote data area are all surrounded by another common shield (shown) and also are enclosed in a grounded conduit (not shown).

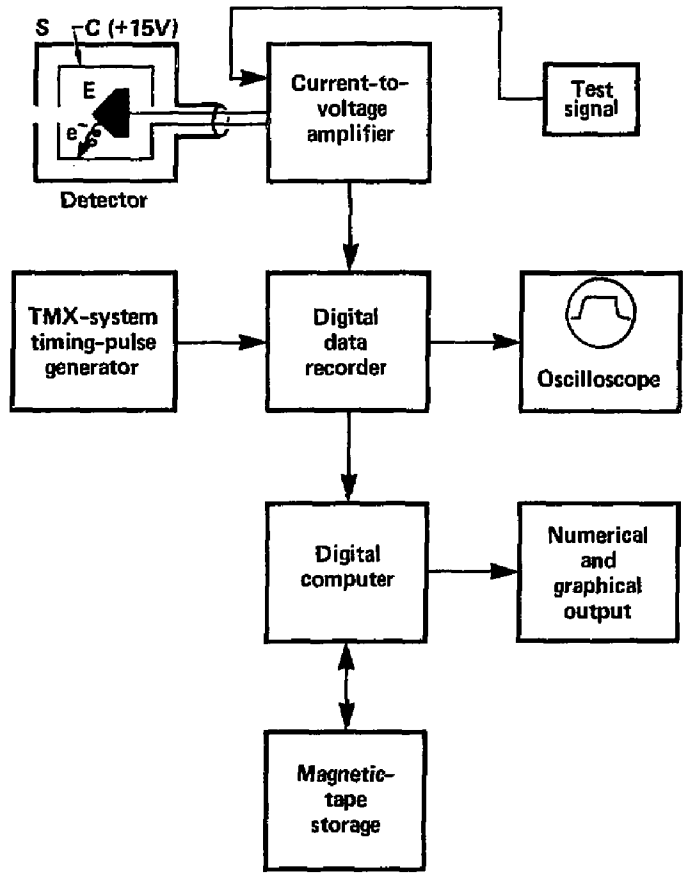

FIG. 10. Block diagram showing elements of beam-attenuation detector and main components of the electronics system.

2.2. Procedure

A representative sequence of events for a TMX shot is depicted in Fig. 11. The magnetic field in the experiment was pulsed and was at full level throughout the events shown. The digital-data recorder obtained its 4096 samples at a 100-kHz sampling rate in about 41 ms. It recorded the detector-signal base level before and after all other events occurred. The neutral beam along which a beam-attenuator-detector array was aimed, designated the "diagnostic beam," was turned on before any plasma-forming events in the shot sequence began. This enabled us to obtain an unattenuated signal level for the normalization discussed below. (The diagnostic beam by itself could not build up and maintain the plasma.) The start-up plasma guns were turned on at the same time as the rest of the neutral beams to provide a cold plasma target for trapping the neutral-beam atoms, thus building up an energetic plasma. After this buildup, the plasma guns were no longer needed to sustain the plasma and were turned off. Near the end of the shot, all the neutral beams except the diagnostic beam were turned off. Because the plasma could no longer be sustained, it decayed away. After the diagnostic beam had measured the plasma decay, it too was turned off, leaving only the signal base line to be recorded again.

With the experimental sequence arranged in the manner just described, the attenuation of the diagnostic beam along the various detector lines of sight through the plasma could be determined. To measure the attenuation, we recorded the beam intensity at a detector with and without the plasma being present. A shot during which plasma was formed, called a "plasma shot," followed the sequence shown in Fig. 11. A "reference shot," one without plasma, followed the same sequence except plasma guns and neutral beams other than the diagnostic beam were not turned on. All the rest of the experimental environment was the same except no plasma was formed.

Figure 12(a) shows examples of detector signal level versus shot time for these two types of shots. The difference in the signal levels (i.e., the shaded region) indicates the proportion of the beam intensity attenuated by the plasma. This fractional attenuation versus time is redrawn in Fig. 12(b). This figure shows the plasma buildup when the start-up plasma guns and remaining neutral beams were turned on, some decrease in attenuation after the plasma guns were turned off, and the plasma decay after all neutral beams except the diagnostic beam were turned off.

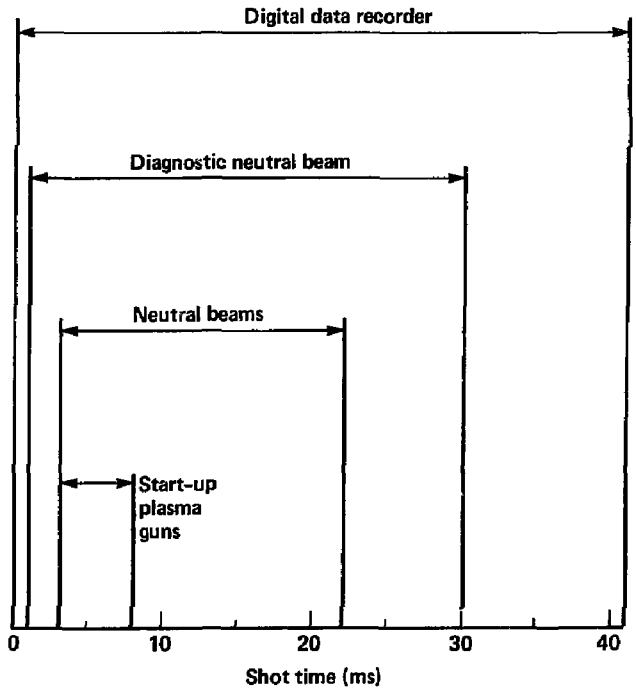

FIG. 11. Sequence of events for a representative TMX shot showing the activation-time intervals for the digital-data recorder of a beam-attenuation-detector signal, diagnostic neutral beam, other neutral beams, and start-up plasma guns.

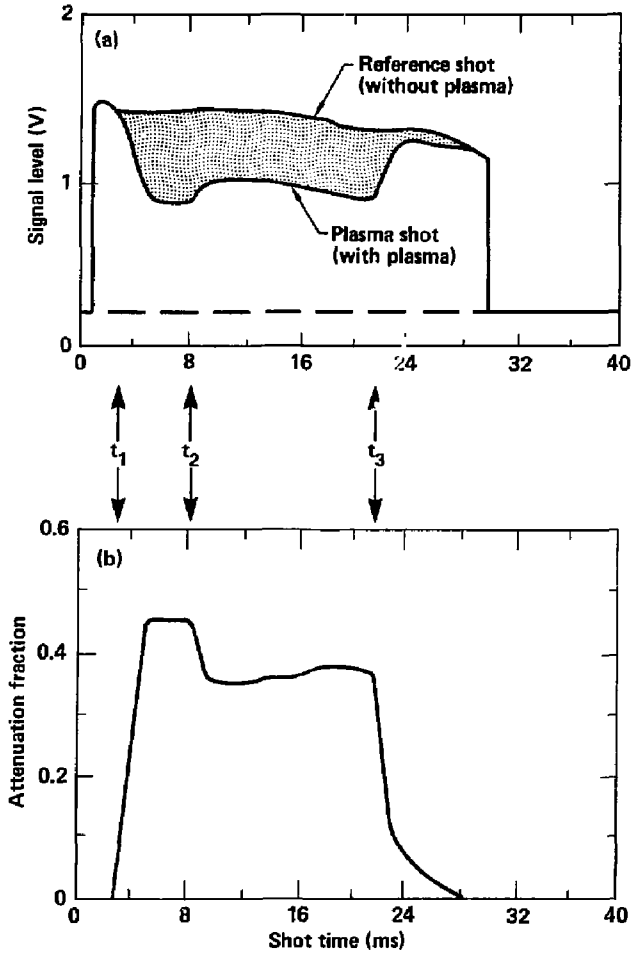

FIG. 12. Example of reference and plasma shots and resulting attenuation. (a) Representative detector signals as a function of shot time with and without plasma being present. (b) Attenuation fraction obtained from the shaded area in (a). The arrows show the turn-on time of the plasma guns and neutral beams (t_1), turn-off time of the plasma guns (t_2), and turn-off time of the neutral beams (t_3). These times correspond to the timing sequence in Fig. 11.

The plasma and reference shots were usually taken close together in time so as to minimize variations in detector calibration and in beam intensity and composition. For a constant detector calibration, the secondary-electron-emission coefficient must remain constant. This coefficient depends on the emitter surface conditions such as composition, contamination, and temperature (e.g., see Ref. [18]). We assumed the surface conditions did not change significantly over a relatively short period of time; for example, we assumed beam heating was not a significant effect. The secondary-electron-emission coefficient also depends on the beam energy and composition. Parameters of the diagnostic-beam source were held as constant as possible over a series of shots. To provide a stable reproducible signal and to reduce beam failure, we derated the diagnostic beam; that is, operated it below its maximum and less reliable level.

In addition to these reproducibility precautions, we "normalized" the signals from a pair of plasma and reference shots to the same level. First, an adjustment was made to eliminate any base-line difference. Then, we began the normalization procedure by calculating the adjustment necessary to shift the plasma-shot signal level to the same level (on the average) as that of the reference shot over a time period when no plasma was present. This time period usually started after the diagnostic beam was turned on and ended before any plasma was produced (within the 1- to 3-ms shot-time inverval of Figs. 11 and 12). We then assumed that the time variation of the beam intensity at the detector would have been the same throughout both shots if no plasma had been present, and we made this calculated fractional adjustment to the plasma-shot signal over its entire duration. This normalization procedure corrected mostly for an overall change in beam level and, to a lesser extent, for a change in detector calibration. This correction, if any, was made to the data of Fig. 12(a).

In practice, we took several plasma shots after each reference shot if the source and beam appeared to be reasonably reproducible. Each set of plasma shots was followed by another reference shot. Thus, as a consistency check, we could normalize a plasma shot against at least two nearby reference shots.

2.3. Accuracy considerations

The accuracy of this diagnostic method depends, first, on the extent to which a measured detector signal is derived from the diagnostic neutral beam and, second, on the premise that attenuation of the signal with plasma present is due to the plasma. Successful interpretation of beam-attenuation measurements requires that spurious signals or extraneous causes of attenuation be small or negligible. We now discuss several possible undesired effects.

Certain plasma emissions can knock off secondary electrons from a detector-emitter plate just as the neutral-beam atoms can, thus creating unwanted signal levels. Examples of such emissions are energetic photons in the ultraviolet and x-ray range and neutral atoms created when plasma ions charge exchange off neutral-beam atoms. These plasma signals were small in 2XIIB and TMX, being emitted into a large solid angle instead of being directed toward the detectors as was the neutral beam. These effects could be checked by turning off the diagnostic beam briefly during a shot while the plasma was present. The detector signals were then observed to drop to low levels, generally into the noise.

In planning the use of beam-attenuation detectors on an experiment, such unwanted signals should be kept in mind. Estimates of these signal levels can be made. During the experiment, the diagnostic beam can be modulated off and on occasionally to check for such spurious plasma signals. One may be able to correct for any remaining signal, if not too large. This beam-modulation procedure also checks for unwanted signals from fueling beams other than the diagnostic beam, such as might arise from small-angle scattering.

Any spurious signal produced directly by the interaction of the diagnostic beam with the plasma will disappear when the diagnostic beam is briefly turned off, so these signals must be estimated in other ways. If the diagnostic beam is only one of several neutral beams, these estimates may be made by occasionally modulating another beam.

A separate check can be made for photons emitted by the diagnostic-beam-source arc chamber, at which the detectors are directly aimed. With arc turned on but with no high voltage to produce a beam of energetic particles, one can check the detector signal level. This spurious signal was found negligible in 2XIIB and TMX.

Besides attenuation in the plasma, the neutral particles in the beam can also be attenuated in other ways, for example by ionization along the beam path from impact on the background gas and on the gas streaming from the beam-source neutralizer. To the extent that this unwanted attenuation is about the same with and without the plasma present, and is relatively small, the effect is not an adverse one. In our experiments, such attenuation appeared to have only a minor influence. If it had been sizable, we would have needed detailed gas-pressure measurements or estimates to correct for it. Similarly, pressure buildup within a detector unit during a shot also appeared to affect the attenuation measurements minimally.

One needs to minimize the effects of detector-signal noise sources because any uncertainty in the signals will be manifested in the accuracy of the derived attenuation fraction. The noise sources include electronics and cabling, environmental (electromagnetic radiation, for example), short-term beam-intensity noise during a shot, and shot-to-shot relatively long-term beam-intensity variations that cannot be eliminated by normalization. Careful electromagnetic shielding and grounding can reduce signal noise. Attention must be paid to the operation of the diagnostic-beam source because proper functioning of this measurement technique requires stable behavior of the emitted neutral beam.

Another way in which detector signals can give inaccurate results is if they become space-charge limited. Then, the beam-intensity variations at the detector are not reliably reproduced, and faulty calculated attenuation fractions result. Assuming zero-velocity electrons leaving the emitter and assuming plane geometry, we have (from Child's law) for the approximate space-charge-limiting electron-current density [19],

$$j \approx 2.33 \times 10^{-6} V^{3/2}/d^2 \quad ,$$

where j is in amperes per square centimeter, V is the applied voltage between emitter and collector in volts, and d is the distance between emitter and collector in centimeters. If the secondary-electron current becomes significantly greater than this estimate, then the electrostatic potential produced by the secondary-electron cloud may begin to reduce the collected fraction of the emitted current. For the TMX end-cell beam-attenuation detector with the peak signal (see Sec. 3.1), the measured current density (averaged over the area of the emitter that has an unobstructed line of sight

through both collimating holes) was about 1 mA/cm^2. This value is close to the space-charge limit estimated from the above equation for $V = 15$ V and $d = 0.36$ cm, where 0.36 cm is the average distance between emitter and collector along the estimated magnetic-field direction at the detector. Signals from other TMX detectors were further below this estimated space-charge limit. (The calculated space-charge limit when cylindrical geometry is assumed [19] gives a larger safety factor.) To increase the space-charge limit, one can increase the detector bias. Alternatively, the current density can be decreased, for example, by placing a screen across the detector entrance hole to decrease the incoming neutral-particle flow.

The various factors discussed here that affect the accuracy of this diagnostic method should be considered, along with the spatial resolution needed, in designing a detector system. Compromises may be necessary. For example, a highly collimated detector configuration provides good spatial resolution and reduces unwanted signals from other fueling beams, but the collimation cannot be so restrictive that the resulting low signal levels become comparable to the electromagnetic and environmental noise levels. Also, it is advantageous for the detector field of view to fall almost entirely on the source-extractor area. As the field of view grows and begins to fall partly outside this area, the beam signal does not increase as rapidly as the spurious plasma signals, so this "signal-to-noise" ratio decreases. A judicial choice of collimating-hole area and spacing can help in adjusting the field of view and signal level of a detector for optimum performance.

If the plasma ultraviolet signal still appears to be a problem, even with optimal design, orienting the detector emitter plate so that the incoming photons and neutral particles strike near grazing incidence will help emphasize the neutral-particle signal compared with the photon signal. This occurs because the secondary-electron coefficient for the neutral particles increases and that for the photons decreases with increasing angle of incidence from the surface normal (e.g., see Refs. [20,21]).

To successfully interpret the results of the beam-attenuation diagnostic technique, the measurements should not significantly affect the plasma being observed. This nonperturbation is achieved when measuring the remnants of a fueling beam. If a special diagnostic beam is used for these measurements, then care must be taken to avoid perturbing the plasma. For example, the beam aiming and energy might be chosen so that the ionized beam particles cannot

remain in the plasma, as was the case in the central cell of TMX. Or, if the ions produced are trapped in the plasma, their effect can be minimized by lowering the average beam-current level, either in steady state or by modulation.

A possible way to increase the accuracy of the beam-attenuation measurements and to reduce the number of needed reference shots is to place a beam-monitoring detector between the neutral-beam source and the plasma region in a nonperturbative position. The signal to this detector would not be influenced by the plasma. To the extent that the reproducibility in amplitude and time of this detector signal would indicate the reproducibility of the portion of the beam traveling toward each individual detector in the array (to be determined experimentally without plasma), then this detector would show whether or not the last reference shot was still valid for data reduction. Beam reproducibility might be additionally checked by monitoring certain current and voltage parameters of the neutral-beam source.

3. MEASUREMENT RESULTS AND INTERPRETATION

3.1. Detector-signal level

Figure 13 shows representative unattenuated detector-signal levels measured with an array of beam-attenuation detectors on a TMX end cell. The current-level values for the horizontal and vertical sets of detectors are plotted as a function of position of a detector central line of sight at the plasma. Data points are shown for each of the detectors depicted in Fig. 5 except for the upper two extreme vertical detectors. There, the signal level was too low to be measured satisfactorily because of the rapid falloff of beam intensity with increasing angle away from the normal to the neutral-beam-source extractor grid. (If there had been sufficient plasma for these extreme lines of sight to traverse, the neutral beam could have been temporarily reaimed to check this region.)

The horizontal profile in Fig. 13 does not fall off as rapidly as the vertical profile because more of the detectors in that array had lines of sight normal to the extractor-grid plane. We have measured horizontal profiles wider and flatter than the example shown here. The profile shape depends on source characteristics and operating conditions, for example on the amount of focusing.

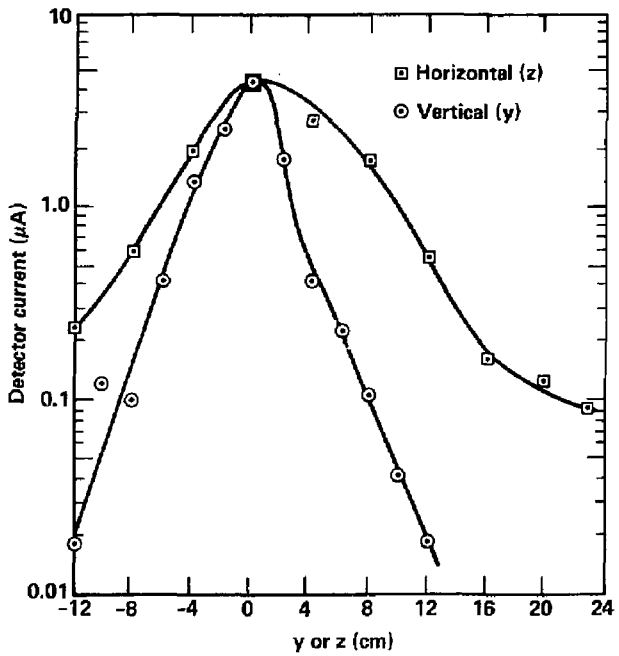

FIG. 13. Representative unattenuated detector-signal level versus position of a detector central line of sight at the plasma (from the horizontal and vertical sets of TMX end-cell beam-attenuation detectors).

It is useful to calculate the peak unattenuated detector signal from the known neutral-beam source parameters and the detector-plus-source configuration. If the computed results agree approximately with the experimental data, one then has a calculational method that can be helpful in designing other detector arrangements. Appendix A shows this calculation for the TMX end-cell configuration. The resulting calculated peak signal of 6.0 μA is in good agreement with the experimental results of Fig. 13.

Recorded signal-noise levels in TMX appeared to be within acceptable limits. The noise level arising from the electronics, cabling, and environmental sources mentioned in Sec. 2.3 was in the 5 to 10 nA range. The signal noise level originating in the unnormalized beam variations was about ±2 to 3% of full signal level. Thus, for the 4.5-μA peak signal of Fig. 13, the beam noise was the more important (about 90 to 135 nA), while the first-mentioned 5- to 10-nA level prevailed for the outer, lower signals of the profiles.

3.2. Calculating line density

The equation that relates the plasma line density to the fraction of the neutral beam attenuated by the plasma is

$$1 - A = T = e^{-\sigma_{eff} \int ndl} , \tag{1}$$

which can be rewritten

$$\int ndl = \frac{- \ln T}{\sigma_{eff}} . \tag{2}$$

Here, A is the fraction of the beam attenuated, T is the fraction transmitted, $\int ndl$ is the integrated plasma density (line density), and σ_{eff} is the effective cross section for the attenuation interactions taking place in the plasma. All these quantities pertain to a chord through the plasma that represents the line of sight for an individual detector.

The experimentally measured quantity in Eqs. (1) and (2) is T, which can be written

$$T = S_p / S_R , \tag{3}$$

where S_p is the detector signal from the neutral beam with the plasma present, and S_R is the detector signal without the plasma present (reference shot).

Signal levels S_P and S_R correspond to a given time during a shot and are the values obtained after making the base-line and normalization corrections discussed in Sec. 2.2. The experimental uncertainty in T, denoted ΔT, can be estimated from

$$\left(\frac{\Delta T}{T}\right)^2 = \left(\frac{\Delta S_P}{S_P}\right)^2 + \left(\frac{\Delta S_R}{S_R}\right)^2 \quad , \tag{4}$$

where ΔS_P and ΔS_R are the absolute experimental uncertainties in S_P and S_R. Sources of these uncertainties were discussed in Sec. 2.3, and some typical TMX values are given in Sec. 3.1.

To convert the experimental measurements of T to line-density results, one needs a value for σ_{eff}. Several types of interactions are involved here, principally charge exchange of beam atoms with plasma ions and ionization of beam atoms by plasma ions and electrons. Plots of the product of cross section times velocity (σv) for these three interactions over the energy ranges pertinent to many controlled-fusion experiments are shown in Fig. 14 [22].

To use these σv results for calculating σ_{eff}, information on plasma and beam parameters is required. For example, we need values for plasma ion and electron energies and the type of ion species present. These may come from other diagnostic measurements, from plasma modeling, or from both. Also needed is the full beam energy and the fraction of the beam atoms at one-third, one-half, and full beam energy. The plasma-parameter values, in particular, may vary with position in the plasma, and thus σ_{eff} may be different for different detector lines of sight through the plasma. Impurity ions in the plasma, unless relatively small, should be taken into account when calculating σ_{eff}.

When calculating σ_{eff}, one needs to allow for the range of possible interaction energies arising from the distribution of energies and from the distribution of directions of motion of the plasma particles colliding with the beam atoms. An integration can be done over the range of particle interactions or an average interaction energy can be assumed from the start so as to simplify the calculations. A σ_{eff} calculation for the TMX end cell is given in Appendix B.

In TMX, we used 1.54×10^{-15} cm^2 for σ_{eff} in the calculations of end-cell line density and assumed the same value for all end-cell detectors.

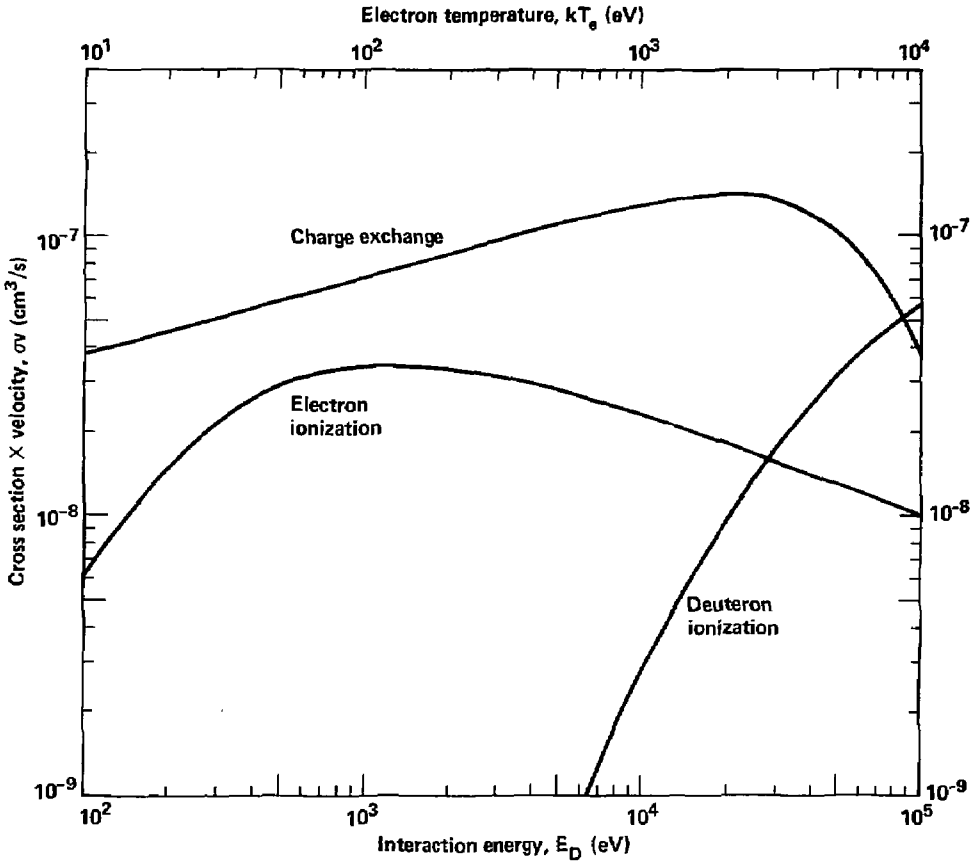

FIG. 14. Product of cross section times velocity (σv) versus interaction energy (or electron temperature) for ionization of incoming deuterium atoms by plasma ions (deuterons) and electrons and for charge exchange off the plasma ions. The electron ionization σv values were obtained by integrating over an electron Maxwellian velocity distribution (electron temperature kT_e given by top horizontal scale). The ion σv results were obtained by taking the cross section for an individual D^+-D^0 interaction at the relative deuteron energy (bottom horizontal scale) and multiplying it by the deuteron velocity corresponding to that energy. To apply these plots to H^+-H^0 interactions, use a σv value for relative deuterium interaction energy twice the relative hydrogen interaction energy (corresponding to the same relative velocity).

Values of plasma and beam parameters used in the σ_{eff} calculation are given in Appendix B. We only considered D^+ plasma ions in this analysis, i.e., plasma impurity ions were assumed to be fractionally low as corroborated by experimental measurements (Ref. [4], Sec. 13). The flatness of the σv plots in the TMX energy ranges (see Fig. 14) helped to minimize the sensitivity of σ_{eff} to the precise values of the plasma parameters used. This helped limit the uncertainty in σ_{eff}, which along with the experimental uncertainty in T contributes to the uncertainty in the calculated line-density values.

A plot of line density versus T for $\sigma_{eff} = 1.54 \times 10^{-15}$ cm^2 is shown in Fig. 15. The TMX line density typically lay in the range 4×10^{13} to 8×10^{14} cm^{-2}, which corresponds to a T range of 94% to 29%. This is a convenient transmission range to measure, with enough attenuation to be out of the noise but not so much attenuation that the transmitted-beam fraction becomes too small to accurately measure or that the sensitivity becomes overly reduced because of the flattening of the curve of line density versus T.

Another experiment might have a different line-density range to measure. Then, adjusting the beam energy or particle species to give a different σ_{eff} value (e.g., see the dashed curve in Fig. 15) may yield more easily measurable values of T, as long as the new beam energy or particle is consistent with the experimental plan.

We estimate that on TMX the electronics and environmental noise, as well as the beam variations that could not be normalized out, caused a typical uncertainty in line density of 1 to 2×10^{13} cm^{-2}, with only minimal special care given to the diagnostic beams. Thus, we were able to measure the typical line-density range mentioned above.

3.3. Experimental line-density profiles

Figure 16 shows representative TMX experimental results for plasma line density obtained from beam-attenuation measurements. Data from all three detector arrays are displayed, including axial and radial (vertical) profiles from the cross arrays in the east-end and west-end cells and a radial profile from the array located near the midplane of the central cell. Measurements from many shots having similar plasma conditions were averaged to give these results. Error bars are the standard deviations of the shot-to-shot variations in the data. The uncertainty in detector line-of-sight axial and radial position is ≤0.5 cm, too small to be conveniently shown on the plots.

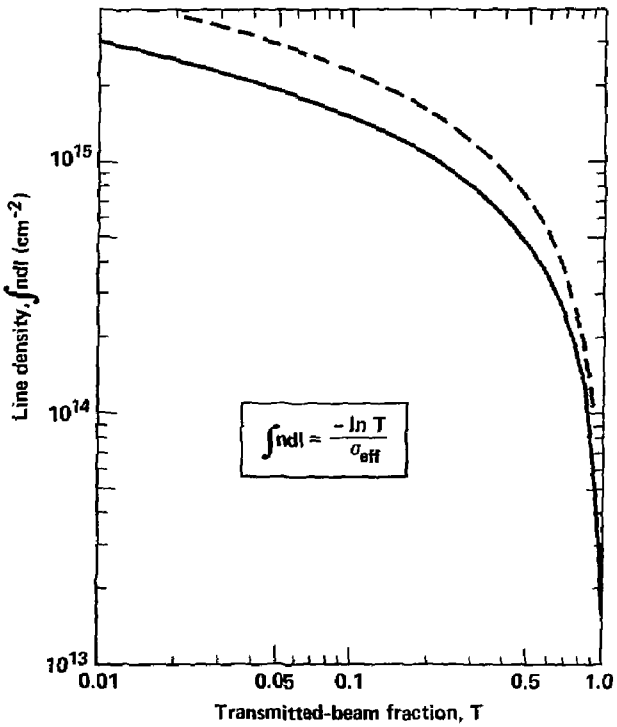

FIG. 15. Line density versus transmitted-beam fraction T for σ_{eff} of 1.54×10^{-15} cm^2 (solid curve, see Appendix B). The dashed curve ($\sigma_{eff} = 1.02 \times 10^{-15}$ cm^2) is obtained with the same assumptions as in Appendix B except the O^+ and O^0 energies are doubled or, equivalently, the energies are unchanged but H^+ and H^0 interacting particles are assumed rather than O^+ and O^0.

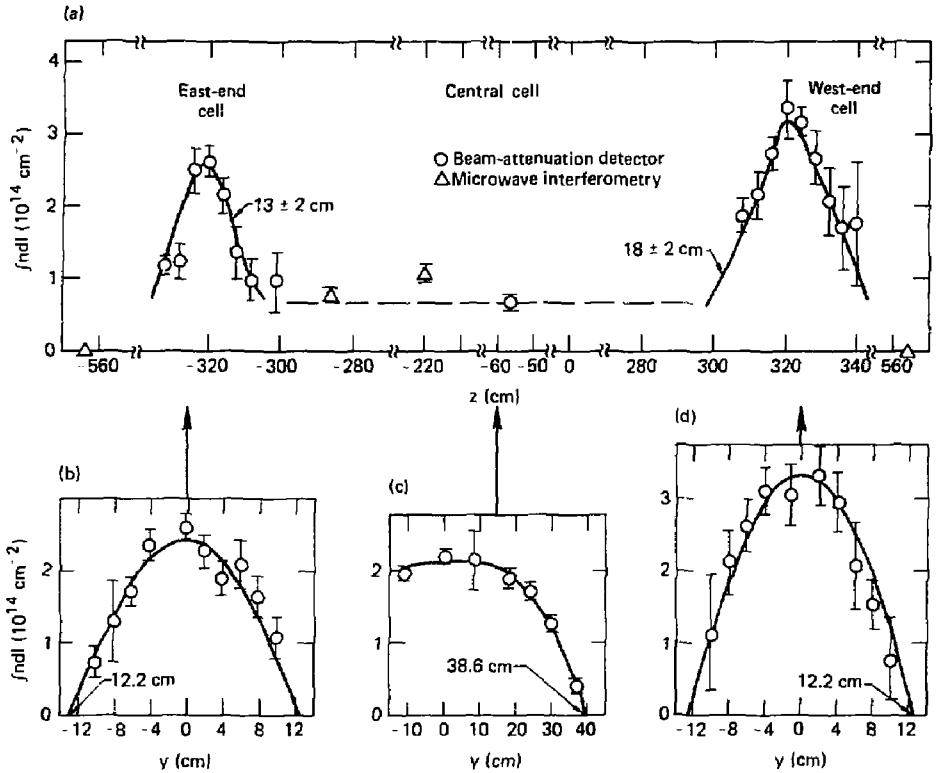

FIG. 16. Plasma profiles of line density showing representative experimental TMX results: Variation along the magnetic axis (a); and vertical (radial) profiles at the midplane of the east-end cell (b), near the midplane of the central cell (c), and at the midplane of the west-end cell (d). All data points in the extended axial profile of (a) have been normalized to the same path length through the plasma as that at the midplane of the end cells. The circles represent data points from the beam-attenuation diagnostic and the triangles, from microwave interferometry. (Note the breaks in the axial scale--the central cell is much longer than either end cell.)

Characteristic axial 1/e falloff lengths given in Fig. 16 are from Gaussian least-squares fits to the data. The radial profiles show parabolic fits to the end-cell data and a higher-order polynomial fit to the central-cell points (see Sec. 3.4), with cutoff radii indicated.

Confidence in the results of beam-attenuation measurements, such as those in Fig. 16, is gained from the consistency of the data and the agreement with theory. An example is the agreement with the microwave-interferometry results. Besides those data points shown in Fig. 16, microwave line-density measurements were also obtained at the midplanes of the end cells. These data usually agreed with the beam-attenuation results to within 20%. Another satisfactory comparison is the qualitative agreement of the theoretical axial plasma-density profile in Fig. 1 with the experimental axial line-density profile in Fig. 16. We observed the normalized end-cell line density to decline smoothly to the central-cell value, as expected from calculations. In yet another comparison, the values of the experimental cutoff radii of the end and central cells agree according to the expectations of magnetic-flux conservation (i.e., $\pi r^2 B$ = constant, where B is 10 kG and 1 kG in the end and central cells, respectively). (An electrically grounded metallic limiter in the central cell, with inner edge at about 38.6 cm, restricted the plasma radius.) Even the higher peak line density in the west-end cell compared with the east-end cell is reasonable because of the somewhat different neutral-beam-trapping configurations in the two locations.

3.4. Inverting to density distributions

A final step in the analysis of the beam-attenuation data is to estimate radial- and axial-density distributions from the line-density-profile data. To obtain a radial-density profile, our customary procedure has been to perform a least-squares fit of the line-density vertical-distribution data with a simple analytic form, to assume cylindrical symmetry of the density distribution around the magnetic axis, and to perform an Abel inversion (e.g., Ref. [23]) of the fit.

In Fig. 17 we show a radial-density profile obtained by this procedure. The solid-line fit to the central-cell line-density data of Fig. 16(c) is a polynomial of the form

$$\int n dl = A[1 - (y/R_c)^2] + B[1 - (y/R_c)^4] \quad , \qquad (5)$$

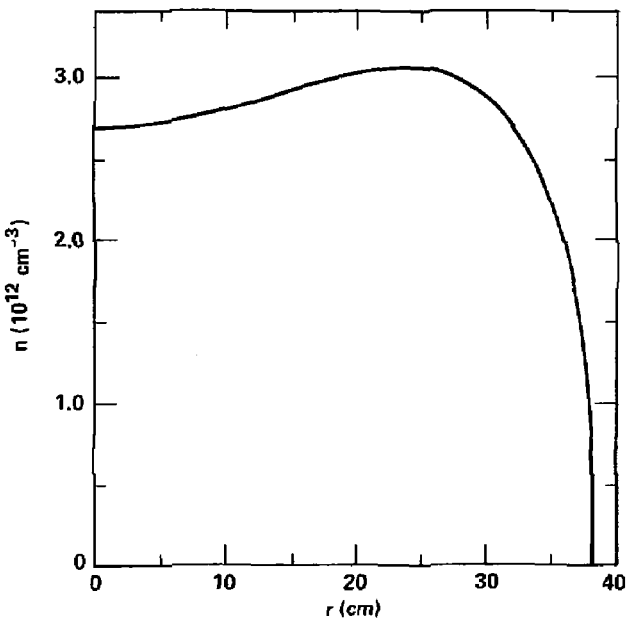

FIG. 17. Example of radial-density profile for the TMX central-cell plasma. The profile was obtained by Abel inversion of a least-squares polynomial fit to the central-cell line-density data of Fig. 16(c).

where $A = 0.7 \times 10^{14}$ cm^{-2}, $B = 1.4 \times 10^{14}$ cm^{-2}, $R_c = 38.6$ cm (cutoff radius), and y is the distance of closest approach to the magnetic axis, in the vertical direction, of a chord through the plasma. An Abel inversion of Eq. (5) yields

$$n(r) = \frac{2}{\pi R_c} [A + 2/3\ B + 4/3\ B(r/R_c)^2] [1 - (r/R_c)^2]^{1/2} \quad , \qquad (6)$$

where r is the radial distance from the magnetic axis. The radial-density variation obtained from the inversion of the fit in Fig. 16(c) is that shown in Fig. 17. Flattening of the line-density profile near y = 0 has led to a radial-density variation with a depression at r = 0.

Examples of other simple functional fits to line-density data are parabolic and Gaussian. The fits to the vertical profiles, shown in Fig. 16, of the east-end and west-end cells are parabolic fits, which have the form

$$\int n dl = A[1 - (y/R_c)^2] \quad , \qquad (7)$$

where $A = 2.42 \times 10^{14}$ cm^{-2} for the east-end cell, $A = 3.30 \times 10^{14}$ cm^{-2} for the west-end cell, and $R_c = 12.2$ cm for both. This is Eq. (5) with $B = 0$, and inverts to Eq. (6) with B = 0, giving peak densities on the magnetic axis of 1.26×10^{13} cm^{-3} in the east-end cell and 1.72×10^{-13} cm^{-3} in the west-end cell. A Gaussian line-density fit,

$$\int n dl = D\ e^{-(y/R)^2} \qquad (8)$$

is convenient to use, when appropriate, because it inverts to a Gaussian radial-density distribution with the same characteristic radius as the line-density Gaussian fit,

$$n(r) = \frac{D}{\sqrt{\pi}\ R} e^{-(r/R)^2} \quad . \qquad (9)$$

Our estimate of the axial-density profile that corresponds to the line-density data of Fig. 16(a) has a similar axial variation as the line-density data but has a change in vertical scale. The peak density in each end cell, located approximately at its midplane, is the peak value obtained in the radial-profile inversion. Other beam-attenuation axial data points in Fig. 16(a) for each end cell are proportionally scaled, having already been normalized to the same plasma path length as that at the midplane

of the end cell. The central-cell axial-density data point is the on-axis value obtained from the central-cell line-density inversion [Fig. 17]. The plotted line-density points from microwave interferometry are scaled in the same proportion as the axial data points for the east-end cell, having been also already normalized to the same plasma path length.

When the radial-profile line-density data are sufficiently extensive and complete, the data can be inverted first and then a least-squares fit of the density results themselves obtained. A matrix-inversion technique can be useful here [24]. Whether the fit is done before or after the inversion, the uncertainties in the line-density data are propagated and amplified in the inverting process and must be kept in mind when interpreting the density results.

Fewer assumptions about the plasma distribution are needed when inverting to a density distribution if several arrays of detectors can be arranged to measure line densities along sets of chords from various positions around the plasma. An example of this is discussed in Ref. [25].

4. CONCLUDING REMARKS

We find that observing neutral-particle-beam attenuation in a controlled-fusion experimental plasma is an extremely useful diagnostic technique. Line-density measurements along an array of chords through the plasma produce important data about the plasma. Spatial information derived from these measurements (e.g., characteristic radial and axial plasma dimensions) is useful in describing and diagnosing the plasma. Values of plasma radius and axial length, and their changes during an individual shot and from shot to shot, are good monitors of plasma formation, steady-state operation, and ambient conditions (such as neutral gas impinging on the plasma and eroding its surface). The magnitudes of the line density and density, as well as their spatial distributions, are also obtained. In addition, from the measured loss of beam current through attenuation, we can directly calculate input power to the plasma from the diagnostic beam and, by inference, can obtain the total power input to the plasma from all beams.

An axial-density distribution measured by a beam-attenuation-detector array provides an experimental handle on the angular distribution function of the plasma particles [26]. This occurs because of the one-to-one

correspondence between a particle's pitch angle in velocity space and the magnetic-field magnitude (related to z) at which the particle is reflected by the mirror. Because a particle spends most of its time in the vicinity of its turning points, the distribution of turning points is very nearly the spatial distribution of density. The angular-distribution function $g(v)$ at the plasma midplane and the spatial-density distribution $n(B)$ are related by an Abel transform.

Correlation of low-frequency fluctuations in the signals from various detectors in an array and from detectors in different arrays can provide information on macroscopic motion of the plasma. Useful data about the TMX plasma were obtained in this way when signal variations in the 10-kHz range were studied [27].

We have used digital computers extensively to acquire, store, and analyze the data from the beam-attenuation-detector arrays (Ref. [4], Appendix B). Thus, we can conveniently process data from a large number of detectors and from many plasma shots, with samples at many times per shot from each detector. The speed of the computer is essential in handling all these data and in performing the calculations discussed in Secs. 2 and 3, such as base-line adjusting, normalizing to the reference shot, calculating the line density at each sample time, and subsequently inverting to a spatial density distribution. The computer system also produces the various types of plots and numerical tabulations needed.

Much of the data processing and analysis is done between shots, and the results are displayed in numerical and graphical form to aid in monitoring the plasma and in making decisions for the subsequent experimentation. Further computer analysis performed during periods when the experiment is not operating and when more detailed and extensive analysis can be done aids in understanding the experimental plasma in general and helps in planning further experiments that may lead toward the goal of controlled thermonuclear fusion.

ACKNOWLEDGEMENTS

We wish to acknowledge the careful mechanical design and construction of the detecting apparatus by N. P. Lund, T. J. Watson, and J. D. Williams, and the competent electronics assistance by A. F. Hinz and F. R. Upper. Also appreciated is the computer programming performed by D. M. Bell and G. Friedman and the encouragement and support of F. H. Coensgen and T. C. Simonen.

APPENDIX A
CALCULATING DETECTOR-SIGNAL LEVEL

The peak unattenuated signal for the TMX end-cell beam-attenuation-detector configuration can be estimated from

$$I_{det} \approx \left(\frac{d^2I}{da\ d\Omega}\right)_{beam} a'\ \Delta\Omega_{det}\ \gamma \quad , \tag{A1}$$

where

$\left(\frac{d^2I}{da\ d\Omega}\right)_{beam}$ = beam current (neutral equivalent) emitted by the neutral-beam-source extractor grid in the normal direction, per unit area, and per unit solid angle,

a' = average area of extractor grid viewed by any point at the rear collimating hole of the detector,

$\Delta\Omega_{det}$ = solid angle of rear collimating hole of detector as seen by the extractor grid,

and

γ = secondary-electron coefficient for the detector emitter plate.

For the TMX detector-plus-source configuration, we calculate

$$\left(\frac{d^2I}{da\ d\Omega}\right)_{beam} \approx \frac{I}{a\Omega} \approx 85.0\ \frac{A}{cm^2\ -\ sr} \quad ,$$

where

I = total beam current (neutral equivalent) ≈ 25 A,

a = total extractor-grid area ≈ 7 cm x 35 cm (from Sec. 2.1),

and

Ω = forward solid angle defined by the 1/e source divergence angles of 0.5° and 2.5° (from Sec. 2.1)

$\approx \pi(0.5)(2.5)/(57.3)^2 = 1.20 \times 10^{-3}$ sr.

We also have:

$a' \approx \pi(1.27)^2 = 5.1\ cm^2$, where the detector field of view is shown in Fig. 4,

$\Delta\Omega_{det} \approx \pi(0.025)^2/(533.5)^2 = 6.90 \times 10^{-9}$ sr (see Fig. 4),

and

$\gamma \approx 2.0$ for an emitting surface that receives no special cleaning, assuming an incident particle energy in the 8- to 16-keV range [18].

Substituting these numbers into Eq. (A1), we obtain $I_{det} \approx 6.0\ \mu A$, the number quoted in Sec. 3.1.

APPENDIX B.
CALCULATING σ_{eff}

The value of 1.54×10^{-15} cm^2 for σ_{eff}, which was used in the analysis of the TMX end-cell beam-attenuation data (Sec. 3.2), was obtained as described here. We assumed 12 keV for the mean plasma D^+ energy, and 100 eV for the electron temperature (kT_e). A maximum beam energy of 16 keV was used, with 60%, 30%, and 10% of the beam D^0 atoms at full, one-half, and one-third beam energy, respectively.

We calculated σ_{eff} by using an average energy E_T for the interaction between each energy component of the incoming beam atoms and the plasma ions. A 90^0 atom-ion collision was assumed typical, so $E_T = E_{beam} + E_{ion}$, where $E_{ion} = 12$ keV, the mean ion energy. The subsequent σ_{eff} calculation is summarized in Table I. The three computed σ_j values (for the three beam-energy components) in the last column of the table, along with the f_j values, were inserted into the equation

$$T = e^{-\sigma_{eff}\int ndl} \approx f_1 e^{-\sigma_1\int ndl} + f_2 e^{-\sigma_2\int ndl} + f_3 e^{-\sigma_3\int ndl} .$$

A σ_{eff} value was then calculated that best satisfied this equation over the range of expected experimental $\int ndl$ values, with 1.75×10^{-15} cm^2 giving good agreement for TMX.

An earlier and more detailed analysis, involving an integration over ion energy and angle and using 2XIIB experimental ion-distribution data, gave a value of σ_{eff} about 12% lower than that obtained using the foregoing simpler method. This factor is included here to obtain the value of 1.54×10^{-15} cm^2 used for analyzing the TMX end-cell data.

TABLE I. CALCULATION OF σ_{eff}.

Beam component, j	Fraction of D^0 beam, f_j	Beam-component energy (keV)	Beam-component velocity, v_j (cm/s)	E_T (keV)	σv (cm^3/s)[a] Charge exchange at E_T	Ionization by ions at E_T	Ionization by electrons at kT_e = 700 eV	$\Sigma\sigma v$ (from the last three columns) (cm^3/s)	$\frac{\Sigma\sigma v}{v_j} = \sigma_j$ (cm^2)
1	0.60	16	1.25×10^8	28	1.38×10^{-7}	1.6×10^{-8}	3.4×10^{-8}	1.88×10^{-7}	1.50×10^{-15}
2	0.30	8	0.88×10^8	20	1.40×10^{-7}	1.0×10^{-8}	3.4×10^{-8}	1.84×10^{-7}	2.09×10^{-15}
3	0.10	5.3	0.72×10^8	17.3	1.39×10^{-7}	0.8×10^{-8}	3.4×10^{-8}	1.81×10^{-7}	2.51×10^{-15}

[a]Values obtained from Fig. 14.

REFERENCES

[1] COENSGEN, F. H., CUMMINS, W. F., LOGAN, B. G., MOLVIK, A. W., NEXSEN, W. E., SIMONEN, T. C., STALLARD, B. W., TURNER, W. C., Phys. Rev. Lett. 35 (1975) 1501.

[2] COENSGEN, F. H., CUMMINS, W. F., GORMEZANO, C., LOGAN, B. G., MOLVIK, A. W., NEXSEN, W. E., SIMONEN, T. C., STALLARD, B. W., TURNER, W. C., Phys. Rev. Lett. 37 (1976) 143.

[3] COENSGEN, F. H., ANDERSON, C. A., CASPER, T. A., CLAUSER, J. F., CONDIT, W. C., CORRELL, D. L., CUMMINS, W. F., DAVIS, J. C., DRAKE, R. P., FOOTE, J. H., FUTCH, A. H., GOODMAN, R. K., GRUBB, D. P., HALLOCK, G. A., HORNADY, R. S., HUNT, A. L., LOGAN, B. G., MUNGER, R. H., NEXSEN, W. E., SIMONEN, T. C., SLAUGHTER, D. R., STALLARD, B. W., STRAND, O. T., Phys. Rev. Lett. 44 (1980) 1132.

[4] TMX GROUP, Simonen, T. C., Editor, Summary of Results from the Tandem Mirror Experiment (TMX), Lawrence Livermore National Laboratory, Report UCRL-53120 (1981).

[5] TURNER, W. C., MOLVIK, A. W., WILLIAMS, J., Bull. Am. Phys. Soc. 21 (1976) 857.

[6] MOLVIK, A. W., COENSGEN, F. H., CUMMINS, W. F., NEXSEN, W. E., Jr., SIMONEN, T. C., Phys. Rev. Lett. 32 (1974) 1107.

[7] FOOTE, J. H., Bull. Am. Phys. Soc. 24 (1979) 1018.

[8] FOOTE, J. H., FUTCH, A. H., Bull. Am. Phys. Soc. 25 (1980) 879.

[9] EUBANK, H. P., NOLL, P., TAPPERT, F., Nucl. Fusion 5 (1965) 68.

[10] AFROSIMOV, V. V., IVANOV, B. A., KISLYAKOV, A. I., PETROV, M. P., Sov. Phys.-Tech. Phys. 11 (1966) 63.

[11] AFROSIMOV, V. V., GLADKOVSKII, I. P., Sov. Phys.-Tech. Phys. 12 (1968) 1135.

[12] BEREZOVSKII, E. L., KISLYAKOV, A. I., MIKHAILOV, E. A., Sov. Phys.-JETP Lett. 19 (1974) 166.

[13] KISLYAKOV, A. I., PETROV, M. P., Sov. Phys.-Tech. Phys. 15 (1971) 1252.

[14] FINLAYSON, V. A., COENSGEN, F. H., NEXSEN, W. E., Jr., Nucl. Fusion 12 (1972) 659.

[15] EQUIPE TFR, Nucl. Fusion 19 (1979) 1261.

[16] BAKER, W. R., BERKNER, K. H., COOPER, W. S., EHLERS, K. W., KUNKEL, W. B., PYLE, R. V., STEARNS, J. W., in Plasma Physics and Controlled Nuclear Fusion Research (Proc. 5th Int. Conf. Tokyo, 1974) Vol. 1, IAEA, Vienna (1975) 329.

[17] MOLVIK, A. W., MUNGER, R. H., DUFFY, T. J., CORRELL, D. L., Rev. Sci. Instrum. 52 (1981) 965.

[18] LARGE, L. N., WHITLOCK, W. S., Proc. Phys. Soc. London 79 (1962) 148.

[19] COBINE, J. D., Gaseous Conductors, Dover Publications, Inc., New York (1958) 125.

[20] MORITA, K., AKIMUNE, H., SUITA, T., Jpn. J. Appl. Phys. 5 (1966) 511.

[21] MAKINSON, R. E. B., Proc. R. Soc. London, Ser. A, 162A (1937) 367.

[22] FREEMAN, R. L., JONES, E. N., Atomic Collision Processes in Plasma Physics Experiments, Culham Laboratory, Report CLM-R137 (1974).

[23] GRIEM, H. R., Plasma Spectroscopy, McGraw-Hill, New York (1964) 176.

[24] ALLEN, S. L., in Mirror Fusion Quarterly Report, April through June 1981, Lawrence Livermore National Laboratory, Report UCRL-50051-81-2 (1981) 14.

[25] NAVARRO, A. P., PARÉ, V. K., DUNLAP, J. L., Rev. Sci. Instrum. 52 (1981) 1634.

[26] HALL, L. S., SIMONEN, T. C., Phys. Fluids 17 (1974) 1014.

[27] HOOPER, E. B., HALLOCK, G. A., FOOTE, J. H., Lawrence Livermore National Laboratory, Report UCRL-86589 Rev. 1 (1982); accepted for publication in Phys. Fluids.

3539v/mm

DISCLAIMER

Printed in the United States of America
Available from
National Technical Information Service
U.S. Department of Commerce
5285 Port Royal Road
Springfield, VA 22161
Price: Printed Copy $; Microfiche $3.50

Page Range	Domestic Price	Page Range	Domestic Price
001-025	$ 5.00	326-350	$ 18.00
026-050	6.00	351-375	19.00
051-075	7.00	376-400	20.00
076-100	8.00	401-425	21.00
101-125	9.00	426-450	22.00
126-150	10.00	451-475	23.00
151-175	11.00	476-500	24.00
176-200	12.00	501-525	25.00
201-225	13.00	526-550	26.00
226-250	14.00	551-525	27.00
251-275	15.00	526-550	28.00
276-300	16.00	601-up [1]	
301-325	17.00		

[1] Add 2.00 for each additional 25 page increment from 601 pages up.